Unusual Fermi-Level Pinning and Ohmic Contact at Monolayer Bi_2O_2Se–Metal Interface

Shiqi Liu, Lianqiang Xu, Yuanyuan Pan, Jie Yang, Jingzhen Li, Xiuying Zhang, Lin Xu, Hua Pang, Jiahuan Yan, Bowen Shi, Xiaotian Sun, Han Zhang, Linqiang Xu, Jinbo Yang, Zhiyong Zhang, Feng Pan, and Jing Lu**

Very recently, high-mobility and air-stable 2D semiconductor Bi_2O_2Se has been discovered and believed to be a promising channel candidate for the next-generation field-effect transistor (FET). High-performance few-layer Bi_2O_2Se FETs have been realized due to the existence of ohmic contact between few-layer Bi_2O_2Se and the metal electrodes. However, monolayer (ML) Bi_2O_2Se FET exhibits poor device performance owing to lack of good contact between ML Bi_2O_2Se and the metal electrode. This work simulates the ML Bi_2O_2Se Schottky barrier field-effect transistors with a sequence of common electrodes (Au, Pd, Pt, Ag, Sc, and Ti) for the first time by using ab initio quantum transport simulations. For Ag, Au, and Pd electrodes, a lateral *n*-type Schottky contact is formed with similar Schottky barrier heights of 0.43–0.52 eV due to a strong usual Fermi-level pinning (FLP) to the band gap of ML Bi_2O_2Se. Remarkably, Pt, Sc, and Ti electrodes lead to a desirable lateral *n*-type ohmic contact because of an unusual FLP above the ML Bi_2O_2Se conduction band as a result of electrode work function modification at the interface. Therefore, high performance is anticipated for ML Bi_2O_2Se devices with these low-resistance ohmic contacts.

1. Introduction

With the development of the semiconductor industry, traditional highly mature field-effect transistors (FETs) based on silicon are approaching their limits.[1–3] The performance degradation caused by short-channel effects restricts the further development of transistors. One way to solve this problem is to choose alternative channel materials. With few lateral dangling bonds and atomically uniform thickness, 2D semiconductors could exhibit efficient carrier transport and excellent gate electrostatics.[4–6] These superiorities make them very promising candidates as channel materials for next-generation FETs. However, 2D semiconductors that have both high carrier mobility and air stability are elusive. Among the widely studied 2D semiconductors, transition metal dichalcogenide bears an apparently much lower mobility (200 $cm^2\ V^{-1}\ s^{-1}$),[7] making it hard for the device to achieve high performance. Phosphorene meets high carrier mobility (1000 $cm^2\ V^{-1}\ s^{-1}$) but is unstable in air.[8] It is highly urgent to search 2D semiconducting materials with both high carrier mobility and air stability. Lately, an emerging layered bulk semiconductor Bi_2O_2Se with a layer-dependent band gap of 0.1–1.20 eV has been attracting much attention.[9,10] The large-domain-size ultra-thin Bi_2O_2Se nanoplates grown by CVD has already been fulfilled. The

Dr. S. Liu, Dr. L. Xu, Dr. J. Yang, Dr. J. Li, Dr. X. Zhang, H. Pang, J. Yan, Dr. B. Shi, Dr. H. Zhang, L. Xu, Prof. J. Yang, Prof. J. Lu
State Key Laboratory of Mesoscopic Physics and Department of Physics
Peking University
Beijing 100871, P. R. China
E-mail: jinglu@pku.edu.cn
Prof. J. Yang, Prof. J. Lu
Collaborative Innovation Center of Quantum Matter
Beijing 100871, P. R. China
Prof. F. Pan
School of Advanced Materials
Peking University
Shenzhen Graduate School
Shenzhen 518055, P. R. China
E-mail: panfeng@pkusz.edu.cn

The ORCID identification number(s) for the author(s) of this article can be found under https://doi.org/10.1002/adts.201800178

DOI: 10.1002/adts.201800178

Dr. L. Xu
School of Physics and Electronic Information Engineering
Engineering Research Center of Nanostructure and Functional Materials
Ningxia Normal University
Guyuan 756000, Ningxia, P. R. China
Dr. L. Xu, Prof. Z. Zhang
Key Laboratory for the Physics and Chemistry of Nanodevices and
Department of Electronics
Peking University
Beijing 100871, P. R. China
Dr. Y. Pan
State Key Laboratory of Heavy Oil Processing
Institute of New Energy
College of Chemical Engineering
China University of Petroleum (East China)
Qingdao 266580, P. R. China
Dr. X. Sun
College of Chemistry and Chemical Engineering and Henan Key
Laboratory of Function-Oriented Porous Materials
Normal University
Luoyang, Luoyang 471934, P. R. China

maximum Hall mobility of CVD-grown Bi_2O_2Se flakes is as high as ≈450 $cm^2 V^{-1} s^{-1}$ at room temperature and ≈29 000 $cm^2 V^{-1} s^{-1}$ at 1.9 K.[9] The field mobility of Bi_2O_2Se can even reach 2000 $cm^2 V^{-1} s^{-1}$ for thicker Bi_2O_2Se at room temperature.[9] Besides, Bi_2O_2Se has excellent air stability with thickness even down to monolayer (ML). Both high carrier mobility and air stability render 2D Bi_2O_2Se the very competitive 2D channel material for next-generation FET.[11,12]

In traditional metal-oxide-semiconductor FETs (MOSFETs), part of the channel is degenerately doped and is used as the source and drain. However, a controllable and sustainable substitutional doping method is lacking for 2D materials, and the metal electrode usually has to be directly contacted with the 2D semiconducting channel to inject carriers.[13–15] Schottky barrier is often generated at the metal–2D semiconductor interface (such an FET is named SBFET) and reduces the efficiency of carrier injection.[16–18] Fermi-level pinning (FLP) is chiefly responsible for the Schottky barrier and often derives from metal-induced gap states (MIGS) or Fermi-level modulation by interfacial interaction.[5,16,19,20] The fabricated bilayer (BL) Bi_2O_2Se SBFETs with Au/Pd electrode have good performance because ohmic contact is achieved. By contrast, the ML Bi_2O_2Se FETs have poor performance due to the unsatisfactory contact originating from the sudden enlarged band gap from bilayer to monolayer limit (1.2 eV for ML and 0.2 eV for BL).[9] On the other hand, ML Bi_2O_2Se MOSFETs outperform their BL counterparts in terms of the theoretical simulations.[21,22] Thus, finding a proper metal electrode that can form a low-resistance or a preferred ohmic contact with ML Bi_2O_2Se semiconductor is critical for fabricating high-performance ML Bi_2O_2Se devices.

In this study, the interfacial properties of ML Bi_2O_2Se transistors are explored with Au, Pd, Pt, Ag, Sc, and Ti contacts by using first-principles band structure calculations and quantum transport simulations (QTSs). There is no vertical Schottky barrier at the metal–ML Bi_2O_2Se interface due to band hybridization. The QTSs indicate that a lateral *n*-type Schottky contact is formed in ML Bi_2O_2Se FET with Au, Pd, and Ag contacts due to strong usual FLP and characterized by electron Schottky barrier heights (SBHs) of 0.5, 0.43, and 0.52 eV, respectively. Remarkably, the unusual FLP above the conduction band of ML Bi_2O_2Se is found with Pt, Sc, and Ti contacts due to the work function modification at the source/drain-channel interface via interface dipole induced by charge redistribution. As a result, a desirable lateral *n*-type ohmic contact is generated with Pt, Sc, and Ti electrodes. Therefore, good electrical contact can exist at the ML Bi_2O_2Se–metal interface and a high-performance ML Bi_2O_2Se SBFET can be expected.

2. Experimental Section

The actual stoichiometry of ML Bi_2O_2Se (as channel) in the simulation was $Bi_2O_2Se_2H_2$, as shown in **Figure 1**a. Figure 1a$_1$, 1a$_2$, and 1a$_3$ represent the top, front, and side views of ML Bi_2O_2Se, respectively. Both the top and bottom surfaces were terminated by Se layers to preserve the inversion symmetry of the bulk. Then,

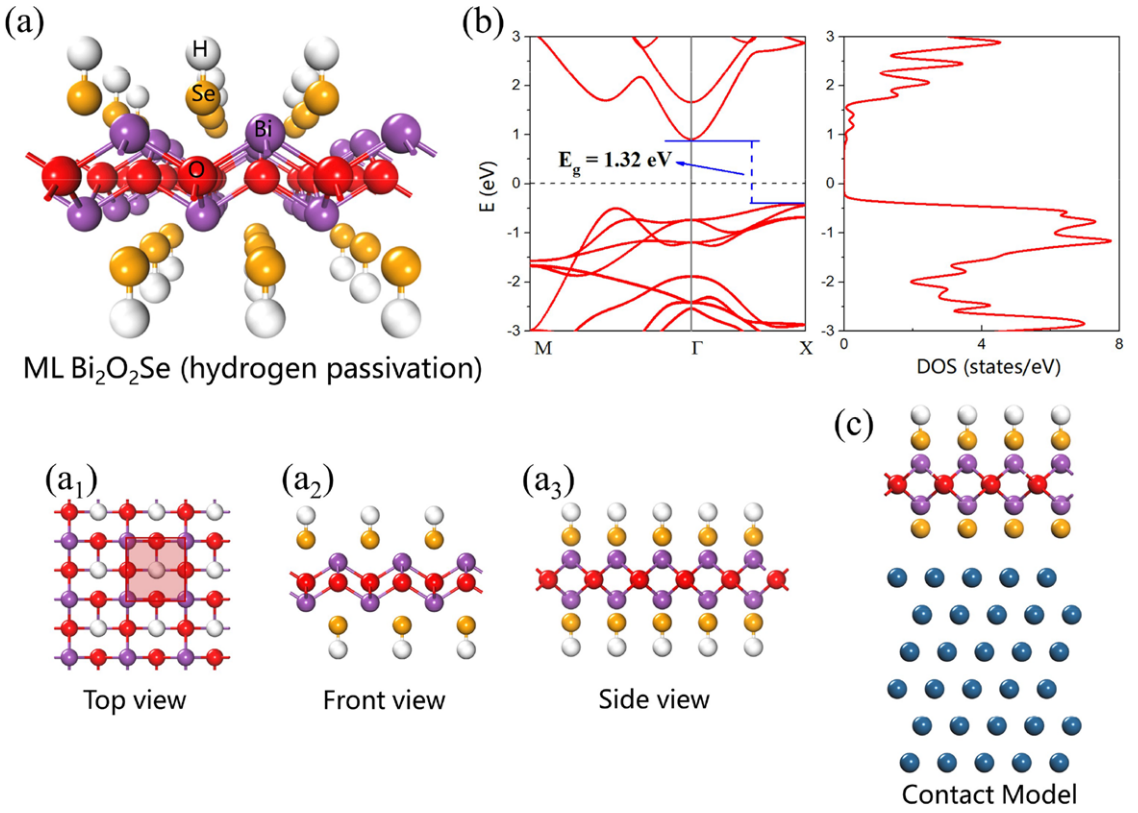

Figure 1. a) Perspective view of free-standing ML Bi_2O_2Se; a$_1$–a$_3$) top, front, and side views of ML Bi_2O_2Se, respectively. The red shadow in (a$_1$) represents a primitive cell. b) Band structure and DOS of ML Bi_2O_2Se. c) Initial configuration of ML Bi_2O_2Se on the metal surface (blue ball).

Table 1. Calculated Interfacial Properties of ML Bi_2O_2Se–Metal Contacts.

Contact	Au	Pd	Pt	Ag	Sc	Ti
$\bar{\varepsilon}$ (%)	4.66	4.60	4.60	4.60	1.30	4.60
d_Z (Å)	2.12	1.73	1.36	1.90	1.94	1.60
$d_{Se\text{-}M}$ (Å)	2.51	2.38	2.45	2.55	2.63	2.46
E_b (eV)	1.62	2.41	1.62	1.72	3.58	3.49
W_M (eV)	5.1	5.12	5.65	4.26	3.5	4.33
$W_{M\text{-}S}$ (eV)	4.65	4.54	4.74	4.18	3.22	3.75
$\Phi^e_{L,W}$ (eV)	1.22	1.11	1.31	0.75	−0.21	0.32
$\Phi^h_{L,W}$ (eV)	0.10	0.21	0.01	0.57	1.53	1.00
$\Phi^e_{L,T}$ (eV)	0.50	0.43	0	0.52	−0.1	−0.05
$\Phi^h_{L,T}$ (eV)	0.70	0.77	1.20	0.68	1.30	1.25

$\bar{\varepsilon}$ is the average lattice constant mismatch between the metal surfaces and ML Bi_2O_2Se. The equilibrium distance d_Z is the average distance between the contact ML Bi_2O_2Se–metal interfaces in the vertical direction. $d_{Se\text{–}M}$ is the minimum atom-to-atom distance from the selenium atoms to the metal atoms. The binding energy E_b is the energy per indium selenide unit (Bi_2O_2Se) required to remove ML Bi_2O_2Se from the metal surface. W_M and $W_{M\text{–}S}$ are the calculated WF for clean metal surface and the ML Bi_2O_2Se–metal system, respectively. $\Phi^e_{L,W}$ ($\Phi^h_{L,W}$) and $\Phi^e_{L,T}$ ($\Phi^h_{L,T}$) are the lateral electron (hole) SBHs obtained from the work function approximation and the quantum transport simulation, respectively.

the outermost Se layers were passivated by hydrogen atoms to balance the non-stoichiometry and stabilize ML Bi_2O_2Se.[9] As for the composite electrode, the interface between the metal and ML Bi_2O_2Se was modeled by putting Au, Pd, Pt, Ag, Sc, and Ti on ML Bi_2O_2Se and removing the hydrogen atoms at the interface. There are two reasons to explain the electrode construction. First, the strong deformation, which is caused by the interaction between hydrogen and the metal, makes it difficult to optimize and obtain stable interface structure. Second, removing the hydrogen atoms at the interface does not influence the coupling between the metal and ML Bi_2O_2Se. Besides, the quick optimization to a stable configuration also proves the rationality of this kind of structure. The initial distance between these two surfaces was set at 3 Å.

The metal was stretched to fit ML Bi_2O_2Se and the contact mismatches were in the range of 1.3–4.66%, as listed in **Table 1**. This series of metals was chosen because they are commonly used in experiments and cover a large scale of work functions (3.5–5.65 eV). There were six layers of metal atoms in the composite system. Based on the previous studies,[23–26] the top three layers were fixed to simulate the bulk metal, while the bottom three layers were free to interact with ML Bi_2O_2Se and made sure the composite system could be relaxed to stable states. ML Bi_2O_2Se had a 1.32 eV indirect band gap without the inclusion of spin–orbital coupling (Figure 1b), which agreed with the one of 1.20 eV of the former DFT calculations.[9] A 15 Å vacuum buffer space was set along the contact directions to ensure decoupling between neighboring slabs. This kind of simulation was guaranteed practical and reliable based on the previous studies.[20,27–30] The metal–ML Bi_2O_2Se composite served as the electrode.

The geometry optimization of the electrode was performed using the projector-augmented wave pseudopotential[31,32] and a plane-wave cut-off energy of 500 eV implemented in the Vienna ab initio simulation package code.[33–35] A Γ-centered grid of 7 × 7 × 1 k-points was used to sample the Brillouin zone in the

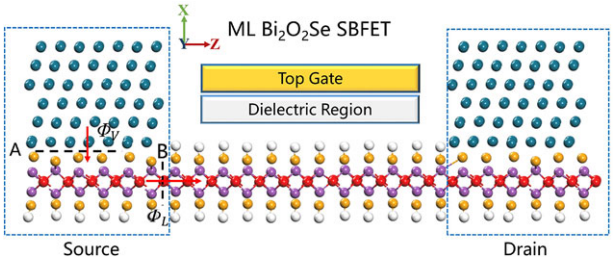

Figure 2. Schematic diagrams of ML Bi_2O_2Se FETs. Black dashed lines denote the interfaces A and B where Schottky barriers may exist. Φ_V and Φ_L represent the vertical SBH and the lateral SBH, respectively. Red arrows represent the pathways that the electrons and holes transfer through the interfaces A and B. The O, H, Se, Bi, and metal atoms are represented by red, white, yellow, purple, and dark green balls, respectively.

structural optimization.[36] The maximum force was less than 10^{-2} eV Å^{-1} per atom, and the energy was converged to within 10^{-5} eV between two successive steps. Due to the van der Waals (vdW) interaction and periodic boundary condition in the vacuum direction, the DFT-D3 method of dipole correction was used to eliminate pseudo interaction.

FET is the critical electronic device, and the gate could modulate the carrier density of the channel and even the SBH despite the existence of a strong FLP at the source/drain-channel interface. Thus, a two-probe model of a ML Bi_2O_2Se SBFET with the semiconducting ML Bi_2O_2Se as the channel and the optimized composite system of metal–ML Bi_2O_2Se as the electrodes was constructed to examine the SBH between ML Bi_2O_2Se and metal electrode. The channel length was chosen as 5 nm, and the detailed reasons are given in Supporting Information.[28,29] The left and right electrodes were semi-infinite. The widely used SiO_2 (dielectric constant = 3.9) was chosen as gate dielectric. The x-, y-, and z-directions of the device (**Figure 2**) took a Neumann-type, a periodic-type, and a Dirichlet-type boundary condition, respectively. The transport properties were calculated by ab initio QTSs based on DFT coupled with non-equilibrium Green's function method and was implemented in the Atomistix ToolKit (ATK) 2017 package.[37–39] Transmission coefficient $T^{k_{//}}(E)$ ($k_{//}$ is a reciprocal lattice vector point along a surface-parallel direction [orthogonal to the transmission direction] in the irreducible Brillouin zone [IBZ]) is calculated as

$$T^{k_{//}}(E) = \mathrm{Tr}\left[\Gamma_L^{k_{//}}(E)G^{k_{//}}(E)\Gamma_R^{k_{//}}(E)G^{k_{//}\dagger}(E)\right] \quad (1)$$

where $G^{k_{//}}$ is the retarded (advanced) Green's function and $\Gamma^{k_{//}}_{L/R}(E) = i(\sum^{r,k_{//}}_{L/R} - \sum^{a,k_{//}}_{L/R})$ represents the level broadening due to the left electrodes and the right electrodes expressed in terms of the electrode self-energies $\sum^{k_{//}}_{L/R}$, which reflects the influence of the electrodes on the scattering region. The transmission function at a given energy $T(E)$ is averaged over different $k_{//}$ in the IBZ. According to the former calculation, single-ξ polarized (SZP) basis set was often accurate enough for bulk metal electrode system, similar for this system. The real-space mesh cutoff was 75 Ha, and the temperature was set at 300 K. The electronic structures of the electrodes and central region were calculated with a Monkhorst–Pack 1 × 32 × 32 and 1 × 32 × 21 k-point grids, respectively.

Generalized gradient approximation (GGA) of Perdew–Burke–Ernzerhof[40] form to the exchange-correlation functional was adopted throughout this paper. Since the doped carriers from metal electrodes greatly screen electron–electron interaction of the 2D semiconductor channel, single-electron approximation becomes a good approximation. Single-electron approximation–based DFT-GGA is effective enough to depict the SBH in an FET configuration.[41,42] Indeed, for a degenerately doped ML $MoSe_2$ at DFT-GGA level, the band gap of 1.52 eV matches well with the renormalized band gap of 1.59 eV obtained by GW method and the experimental result of 1.58 eV.[43] Moreover, the experimental and calculated (in terms of the local density of states [LDOS]) transport gaps of ML, BL, and trilayer (TL) black phosphorene with Ni electrode are 1.00/0.79, 0.71/0.81, and 0.61/0.68 eV, respectively.[20,27,29]

3. Results

3.1. Electronic Structure of the Metal–ML Bi_2O_2Se Interface

The optimized metal–ML Bi_2O_2Se configurations are shown in **Figure 3**. The structure of ML Bi_2O_2Se almost stays unchanged on Au, Pd, Ag, Sc, and Ti electrodes while deforms slightly on Pt electrode. The main parameters of metal–ML Bi_2O_2Se interfaces are listed in Table 1. $\bar{\varepsilon}$ is the average lattice constant mismatch between the metal surfaces and ML Bi_2O_2Se. d_Z is the vertical equilibrium distance between Bi_2O_2Se and the closest metal layer. $d_{Se\text{-}M}$ is the minimum atom-to-atom distance from the selenium atoms to the metal atoms. W_M and $W_{M\text{-}S}$ are the work functions of metal and composite system, respectively. Binding energy E_b is the energy per indium selenide unit (Bi_2O_2Se) required to remove ML Bi_2O_2Se from the metal surface and is calculated as

$$E_b = (E_{Bi_2O_2Se} + E_M - E_{Bi_2O_2Se-M})/N$$

where $E_{Bi_2O_2Se}$, E_M, and $E_{Bi_2O_2Se-M}$ represent the total energy of the pristine ML Bi_2O_2Se, the metal, and the composite system, respectively, and N is the total number of primitive cells (Figure 1a$_1$) in the system. There is strong binding at the metal–ML Bi_2O_2Se interface with an apparent large binding energy E_b, ranging from 1.62 to 3.58 eV and short distance d_Z and $d_{Se\text{-}M}$, ranging from 1.36 to 2.12 Å and from 2.38 to 2.63 Å, respectively.

Though the bonding is strong at these metal–ML Bi_2O_2Se interfaces, there are still differences in the bond strength, which can be explained by the different number of the covalent bonds at the interfaces. The isolated Au ($5d^{10}6s^1$) and Ag ($4d^{10}5s^1$) atoms only form one covalent bond with ML Bi_2O_2Se and thus have the relatively smaller E_b because the outermost orbit is occupied by one unpaired s electron. For the isolated Sc ($3d^14s^2$) and Ti ($3d^24s^2$) atoms whose outer orbits have only one and two unpaired electrons, in fact, the nd and $(n+1)s$ electrons get through a redistribution due to the orbital overlap in the solid form. Therefore, the actual electronic configurations of bulk Sc and Ti turn out to be $3d^24s^1$ and $3d^34s^1$, illustrated by the Mulliken population analysis. For this reason, Sc and Ti form three and four covalent bonds with ML Bi_2O_2Se, corresponding to the larger E_b.

The band structures of the contacts are shown in **Figure 4**, in which the component of ML Bi_2O_2Se (red lines) are extracted from ML Bi_2O_2Se–metal compounds (grey lines). The observed band structure hybridization of ML Bi_2O_2Se in all the systems suggests the intense coupling at the interfaces and is consistent with the strong covalent bonding analyzed before. Based on the

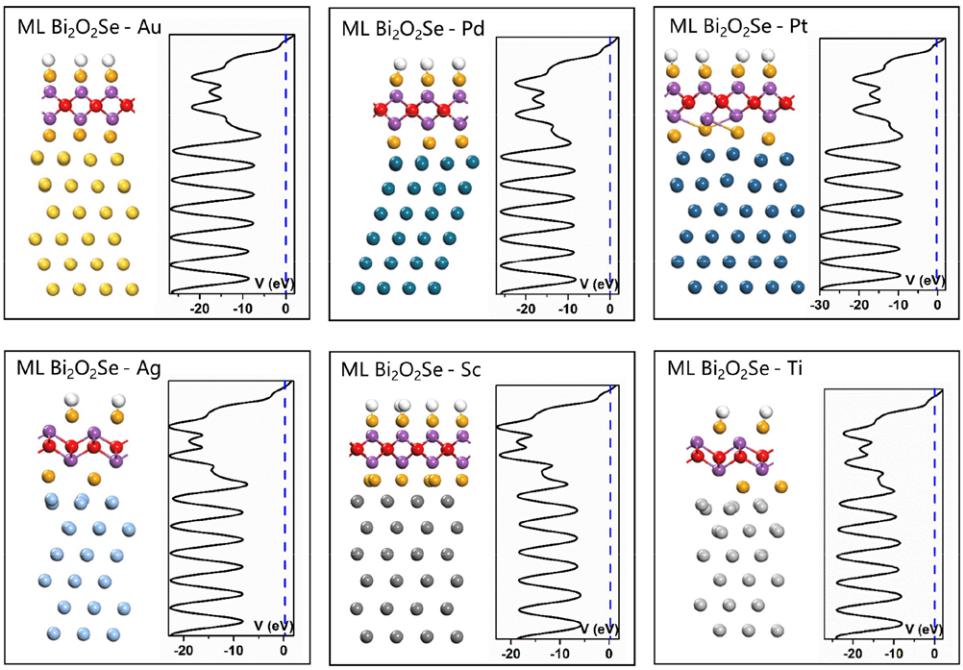

Figure 3. Side view of the optimized structure and average electrostatic potential distribution in planes normal to the interface of ML Bi_2O_2Se on Au, Pd, Pt, Ag, Sc, and Ti surfaces, respectively. The Fermi level is set to zero and denoted by blue dashed line.

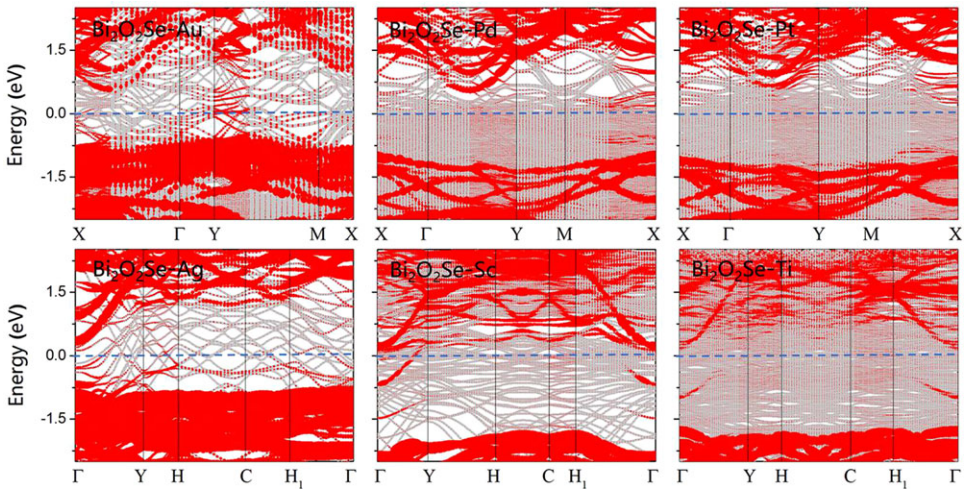

Figure 4. Band structures of the ML Bi_2O_2Se–metal systems. Gray line: Band structure of the total ML Bi_2O_2Se–metal compounds; red line: band structures of the ML Bi_2O_2Se extracted from Bi_2O_2Se–metal compounds. The Fermi level is set at zero energy and denoted by blue dashed line.

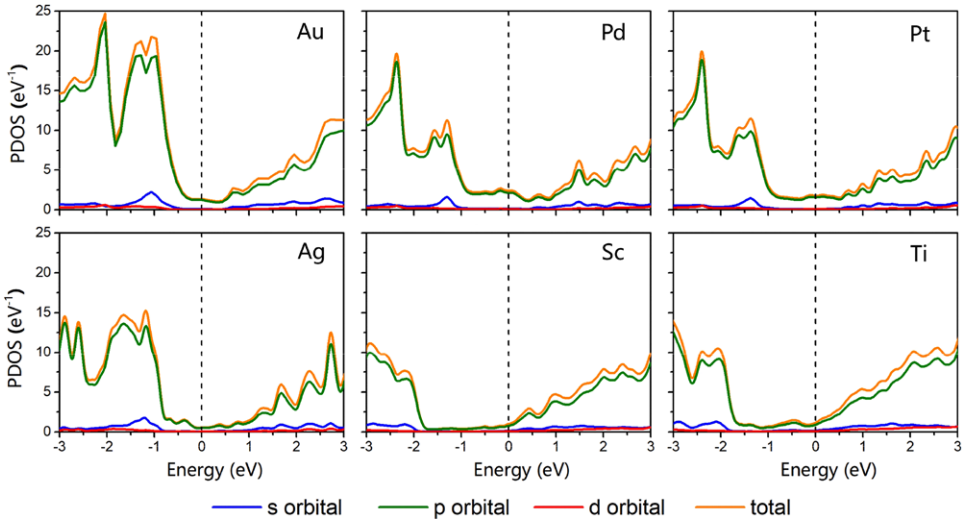

Figure 5. Extracted PDOS of ML Bi_2O_2Se from the energy band calculations of the ML Bi_2O_2Se–metal systems. The Fermi level is set at zero energy and denoted by vertical black dashed lines.

Mulliken population analysis, the partial density of states (PDOS) calculation is taken. PDOS is plotted in **Figure 5** by resolving the contribution of different angular momentum (s, p, d) of the state in the energy spectrum. Around the Fermi level, the states are mainly composed of *p* orbital, matching the outermost electronic structure of Bi ($6p^3$), O ($2s^2 2p^4$), and Se ($4s^2 4p^4$). The pristine ML Bi_2O_2Se band gap all disappears in the metal–ML Bi_2O_2Se systems owing to the hybridization of ML Bi_2O_2Se. Further, the total electron density distributions of the compound systems are plotted in **Figure 6**. There is apparent electron accumulation at the interface with all the chosen metal electrodes, in agreement with the strong covalent bonding and large E_b.

3.2. SBH of the ML Bi_2O_2Se Transistors

In an FET, the Schottky barrier plays an important role. The scattering of the carrier will decrease, the carrier mobility will increase, and the property of a transistor will improve with a lower Schottky barrier. The diagram of the simulated device configuration is shown in Figure 2. Charges transport from the metal electrode to the channel by passing two interfaces and the Schottky barrier can exist at both the two interfaces. One is interface A, which is between the metal and the ML Bi_2O_2Se under the metal. The SBH appearing at interface A is called the vertical SBH. The other is interface B, which is between the source/drain and channel. The SBH appearing at interface B is called the lateral SBH. According to the band structure analyses before, ML Bi_2O_2Se is totally metalized by contacting with metal. Therefore, there is no vertical SBH at interface A for all the interfacial systems. Correspondingly, attention needs to be paid just to the lateral SBH at interface B.

There are two commonly used methods to analyze the SBH of an FET. One is called work function approximation (WFA) in which the electron/hole SBH $\Phi^{e}_{L,W}/\Phi^{h}_{L,W}$ (listed in Table 1) is defined as the energy difference between the Fermi level of

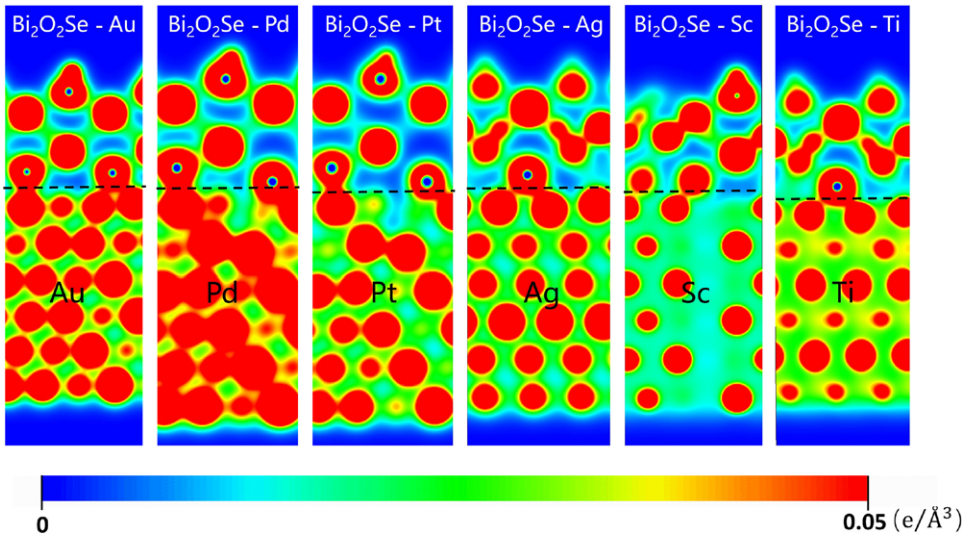

Figure 6. Total electron density distributions of ML Bi_2O_2Se in contact with Au, Pd, Pt, Ag, Sc, and Ti. Black dashed lines denote the interfaces between ML Bi_2O_2Se and the metal.

composite electrode ($W_{M\text{-}S}$) and the CBM/VBM of the pristine ML Bi_2O_2Se channel. The results based on WFA reveal that in the ML Bi_2O_2Se FETs contacted by Sc, lateral *n*-type ohmic contacts are generated with electron SBHs of −0.21 eV. An *n*-type Schottky contact is obtained with a hole SBH of 0.32 eV when the ML Bi_2O_2Se FET is contacted by Ti. Lateral *p*-type Schottky contacts are generated with Au, Pd, Pt, and Ag as electrodes, characterized by holes SBHs of 0.10, 0.21, 0.01, 0.57 eV, respectively. Since this method ignores the interaction between the source/drain and channel, it is believed to be a very crude way to evaluate the lateral SBH in an FET.

By taking the inclusion of the coupling between the electrode and channel into consideration, QTS is capable of determining a more reliable SBH in a simulated FET.[19,20,27,29] The electron/hole SBH ($\Phi^{e}_{L,T}/\Phi^{h}_{L,T}$) can be extracted from the difference between the Fermi level and the CBM/VBM of the channel at the interface B, by means of the local device density of states (LDDOS), which reflect the real space energy band distribution in an FET directly and the MIGS (the newly formed electronic states at the semiconductor's band gap). **Figure 7** shows the LDDOS and the corresponding transmission spectrum of the simulated FETs. The lateral electron (hole) SBHs at the left and right interface of ML Bi_2O_2Se FET with Au electrode are different; the average is taken here. Similar operation of taking average of SBH at the left and right interface has been validated in ML, BL, and TL black phosphorus FETs with Ni electrode.[20,27,29] The results based on QTS reveal that a lateral *n*-type Schottky contact with an electron SBH of 0.50/0.43/0.52 eV is formed at the interface B of the ML Bi_2O_2Se FET with Au/Pd/Ag contact, respectively. Remarkably, a lateral *n*-type ohmic contact with an electron SBH of 0.00/−0.10/−0.05 V is formed at the interface B of the ML Bi_2O_2Se FET with the Pt/Sc/Ti contact, respectively; hence, an ML Bi_2O_2Se FET with a low contact resistance can be obtained. The SBH generated from the LDDOS can also be read by the transmission spectra in the case of Ag contact because the VBM/CBM is flat (Figure 7). The MIGS shown in the LDDOS are abundant and deep into channel in the FET with Ag contact but are inconspicuous for the other contacts.

The doping induced by electrode and the contact polarity from the LDDOS can also be verified by the simulated output and transfer characteristics, as shown in **Figure 8**. According to the output characteristics of the ML Bi_2O_2Se FET with Sc electrode, the current (I_{ds}) increases linearly with the bias voltage (V_b) in the initial stage, indicative of an ohmic contact. From the transfer characteristics, I_{ds} decreases with the increasing negative gate voltage (V_g), suggestive of an *n*-type contact. Taken together, the ML Bi_2O_2Se FET forms *n*-type ohmic contact with an Sc electrode, which is in agreement with the interfacial calculation (in terms of the LDDOS). For the ML Bi_2O_2Se FET with Pd electrode, its output characteristic shows that I_{ds} almost keeps zero in the initial stage and then starts to grow exponentially at $V_b > 0.5$ V, typical of Schottky contact at the source/drain-channel interface. From the transfer characteristic, I_{ds} increases with the growing positive V_g, suggestive of an *n*-type contact. Taken together, the ML Bi_2O_2Se FET forms *n*-type Schottky contact with Pd electrode, a result also in agreement with the interfacial calculation (in terms of the LDDOS).

The SBHs obtained by the WFA and QTS are compared in **Figure 9** and Table 1. For the ML Bi_2O_2Se FET with Au/Pd/Pt/Ag contact, the WFA gives *p*-type contact polarity while the QTS gives *n*-type contact. For the ML Bi_2O_2Se FET with Sc and Ti contacts, though the WFA and QTS give the same *n*-type contact polarity, the SBH differs significantly. When it comes to an investigated FET, previous works tend to give that the WFA prefers generating ohmic contact while the QTS prefers generating Schottky contact. Thus, it really catches attention when the simulated FET with Pt contact shows huge polarity inversion (from *p*-type Ohmlike contact by WFA to *n*-type ohmic contact by QTS), and the simulated FET with Ti contact transforms from *n*-type Schottky by the WFA to *n*-type ohmic contact by the QTS. **Figure 10**a displays the Fermi-level change from pure metal to metal–Bi_2O_2Se compound and then to a device and can be used to explain the SBH discrepancy between the WFA and QTS. When pure metal

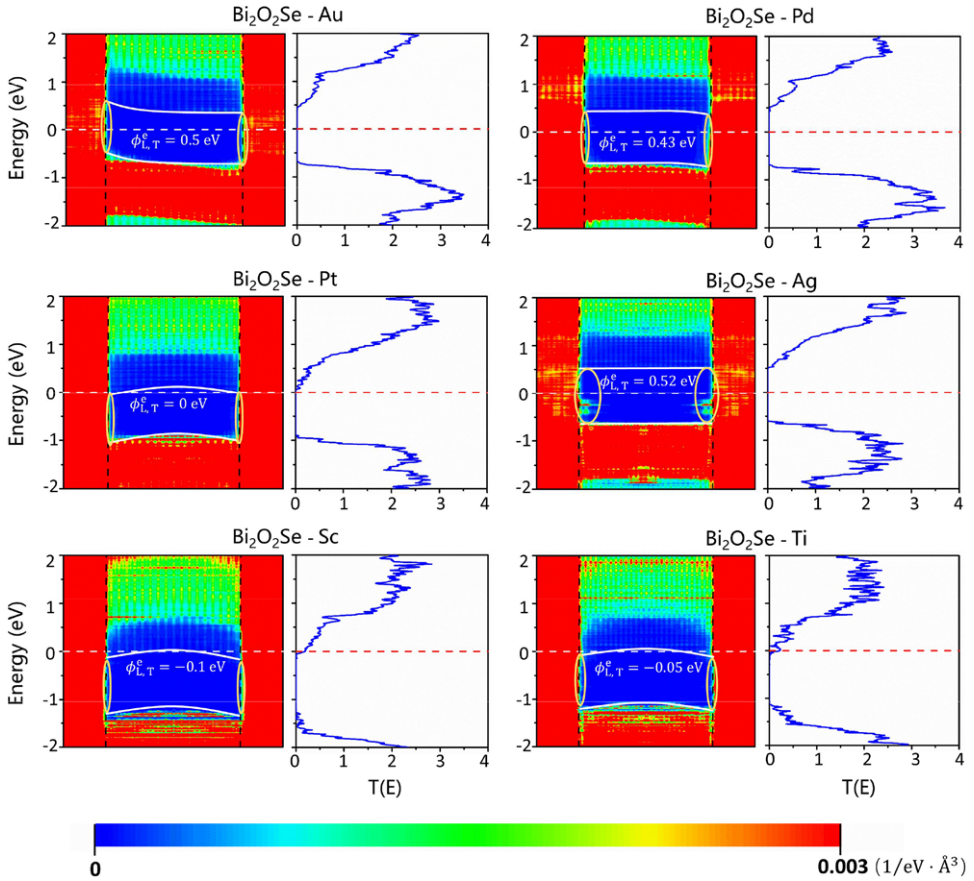

Figure 7. a–f) Zero-bias and zero-gate voltage LDDOS and transmission spectrums of the ML Bi_2O_2Se transistor with a channel length of 5 nm. The conduction band minimum (CBM) and valence band maximum (VBM) are represented by white lines. The Fermi level is represented by a white dashed line in the LDDOS and a red dashed line in the transmission spectrums. $\Phi^e_{L,T}$ and $\Phi^h_{L,T}$ represent the electron SBH and hole SBH in the lateral direction, respectively. The MIGS at the interface of source/drain-channel are circled by the yellow curves. The upright black lines indicate the boundary of the ML Bi_2O_2Se–bulk metal electrode and the intrinsic ML Bi_2O_2Se channel.

and semiconductor contact directly, the Fermi level of the newly founded metal–ML Bi_2O_2Se compound experiences a reformation. In the simulated system, all the Fermi levels are lifted after the formation of metal–ML Bi_2O_2Se compound. This procedure is the first change of the Fermi level.

The second Fermi level change derives from the interaction between the composite electrode and the ML Bi_2O_2Se channel. As far as known, the coupling between the composite electrode and the ML Bi_2O_2Se channel can bring two influences, which leads to the final formed Fermi level. One influence is inducing MIGS. The MIGS serve as a reservoir during the charge transfer between the composite electrode and channel.[44] Because the MIGS are often dispersed at a narrower certain range of energy (smaller than the band gap), the Fermi level is generally more concentrated in a certain area. The apparent MIGS are responsible for the electron SBH of 0.52 eV with Ag contact in Figure 7. The other influence of the composite electrode–channel coupling is to modulate the Fermi level of the metal–ML Bi_2O_2Se compound via interface dipole induced by charge redistribution. This modulation chiefly dominates the lateral SBH when the MIGS at the interface are inconspicuous or fully filled by electrons already. Actually, after the source/drain and channel contacting with each other, the charge redistribution induced by charge repulsion at the contact interface gives rise to a dipole electric field and then modulates the Fermi level of electrode (metal–Bi_2O_2Se compound). The intensity of modulation depends on the formed dipole electric field at different system. Reflected in this system, the Fermi levels of Au/Pd–ML Bi_2O_2Se compounds are modulated within gap, leaving the corresponding FETs in Schottky contact. While the Pt/Ti–ML Bi_2O_2Se compounds' Fermi levels are lifted above the CBM (3.51 eV) of ML Bi_2O_2Se and the corresponding FETs form desirable ohmic contact. Same work function modulations have been observed in the metal–MoS_2 and metal–graphene interfaces.[16,45] On account of the MIGS and/or the Fermi-level modulation influences, the lateral SBHs in an actual device differ greatly from those estimated from the two isolated systems.

FLP within the band gap is common, but for Ti/Pt–ML Bi_2O_2Se compounds, the interfacial dipole modulation even lifts their Fermi level to the channel's conduction band and makes them capable of achieving ohmic contact. This beyond-gap pinning is referred as unusual FLP. Figure 10b displays the lateral electron SBHs derived from the QTS as a function of pristine metal work function. The slope of the fitted line in Figure 10b is defined as pinning factor (S). Because S describes the change of

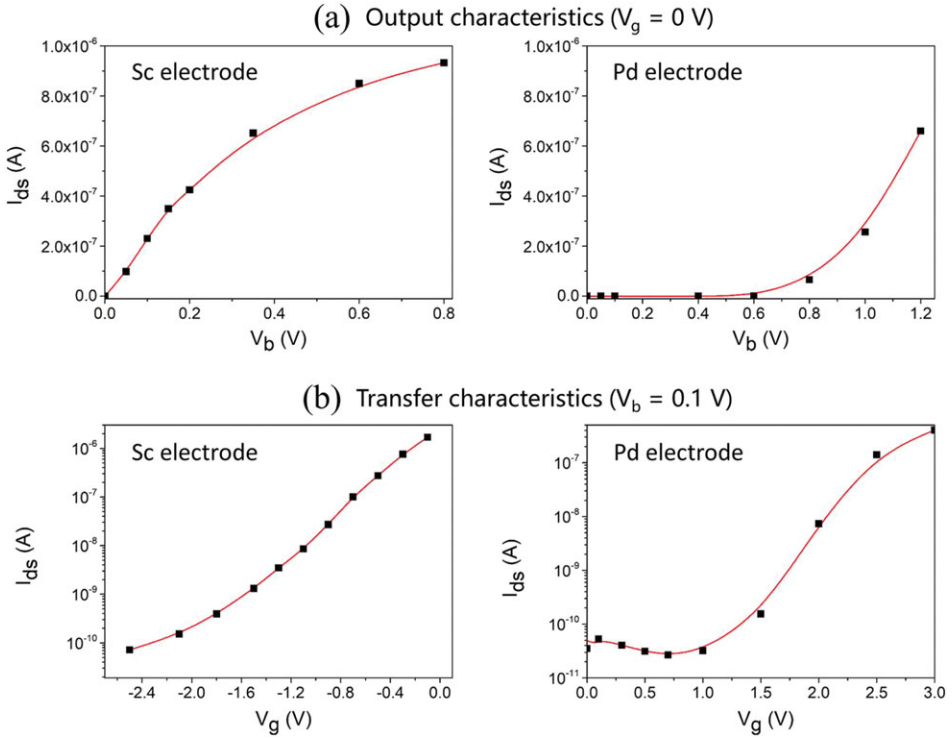

Figure 8. a) Output and b) transfer characteristics of the ML Bi_2O_2Se FET with Sc (*n*-type ohmic contact) and Pd (*n*-type Schottky contact) electrodes, respectively. V_g, V_b, and I_{ds} represent gate voltage, bias voltage, and source–drain current, respectively. The red solid curve is a guidance for the eyes.

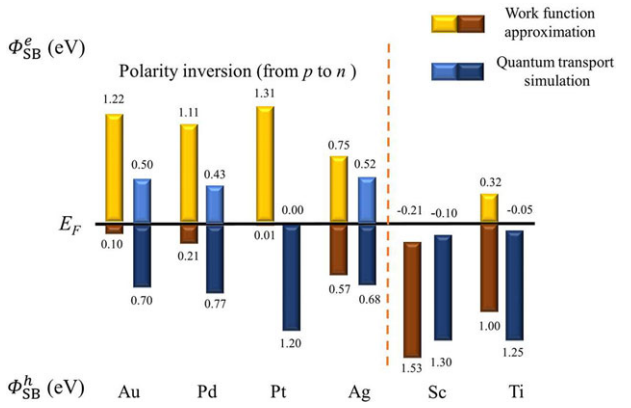

Figure 9. Comparison of the lateral SBHs in the ML Bi_2O_2Se FETs obtained from the work function approximation ($\Phi^{e/h}_{L,W}$) and the quantum transport simulation ($\Phi^{e/h}_{L,T}$).

the electron SBH with the corresponding metal work function, it is used to quantitatively reflect the intensity of FLP ($|S| = 1$ represents no FLP and $|S| = 0$ represents a total FLP).[46] The S of usual within-gap and unusual beyond-gap FLP is −0.07 and 0.05, respectively. The average $\bar{S}$ of FLP is 0.12. All of them point out a strong FLP at the simulated ML Bi_2O_2Se SBFET lateral interface.

4. Discussions

According to the description of the experiment group, they took the Kelvin probe force microscopy measurement of 2D Bi_2O_2Se (5 nm in thickness) to determine its work function for guiding contact metal optimization of device fabrication. The revealing value of ≈5.0 eV (probably also evolving with thickness) matches well with Pd (5.1 eV). Thus, the experiment decided to choose Pd/Au as contact electrodes. The measured Bi_2O_2Se devices all exhibit linear I_{ds}–V_{ds} curves even down to bilayer, suggesting the good ohmic contacts there. The contact resistance is about 5 kΩ μm at 6.2-nm thick Bi_2O_2Se with Au/Pd contact by analyzing the linear I_{ds}–V_{ds} curve.[9] However, for ML Bi_2O_2Se, the experiment still could not achieve good contact. They speculated that the work function mismatch between monolayer crystal and metal electrode and the sudden increase of the band-gap from bilayer (0.20 eV) to monolayer (1.20 eV) together made it hard to form ideal ohmic contact in ML Bi_2O_2Se transistor.

The simulation can prove the difference that the measured BL Bi_2O_2Se transistor with Au/Pd electrode shows ohmic contact[9] while the simulated ML Bi_2O_2Se transistor with Au/Pd electrode turns out to be *n*-type Schottky contact derives from the number of layers. First, the calculated work function of BL and ML Bi_2O_2Se are 4.23 and 4.15 eV, respectively, which means the work function mismatches in ML and BL Bi_2O_2Se–metal are comparable. Second, the DFT calculations for Bi_2O_2Se also reveal a dramatic band gap increase from bilayer (0.43 eV) to monolayer limit (1.32 eV), which is in good agreement with the reported experiment value. Besides, the simulated FET based on bilayer Bi_2O_2Se dose shows an ohmic contact with Au/Pd electrode.[47] Specific contact resistivity of the ohmic contact can also be extracted from the output characteristic and is about 0.24 kΩ μm in the ML Bi_2O_2Se FET with Sc electrode (Figure S2, Supporting Information). As the gate voltage changes from 0 to 1 V, the electron SBH

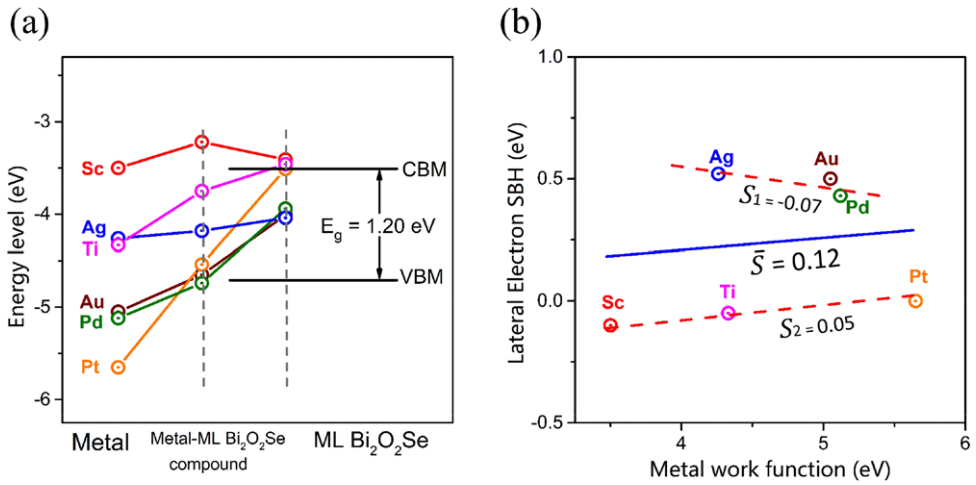

Figure 10. a) Fermi level change from pure metal to metal–Bi_2O_2Se compound and to a device. The gray dashed lines from left to right represent the first change and second change of Fermi level, respectively. b) Lateral electron SBH against the corresponding metal work function for the ML Bi_2O_2Se FETs. S_1 is the usual within-gap FLP factor. S_2 is the unusual beyond-gap FLP factor. $\bar{S}$ is the average FLP factor.

changes from −0.1 to −0.3 eV, as shown in Figure S3, Supporting Information.

The calculated pinning factors of ML tellurene,[48] ML black phosphorene,[29] ML InSe,[49] ML arsenene,[50] and ML blue phosphorene[51] are 0.15/0.09, 0.28, 0.32, 0.33, and 0.42, respectively. The measured pinning factors of ML MoS_2[52] is 0.1. The smaller the pinning factor is, the stronger the FLP existing at the electrode–channel interface. Taking the simulated Ag–ML Bi_2O_2Se contact as an example (Figure 7), the LDDOS shows a lot of deep-into-channel MIGS dispersed at a wide range of energy. Same situation also occurred at the lateral interface of the simulated Ag–ML tellurene FET, corresponding with strong FLP and small pinning factor ($S = 0.15$) analyzed in relevant article.[48] While for InSe, ML arsenene, and ML blue phosphorene, the intensity and depth of MIGS decrease a lot.[50,51] Correspondingly, the FLP is little weaker and the pinning factor ($S =$ 0.23/0.33/0.42) is larger than that in Ag–ML tellurene ($S = 0.15$) and Ag–ML Bi_2O_2Se FET ($S = 0.12$). Thus, it can be inferred that the stronger the FLP, the more robust the SBH, and the smaller the pinning factor.

The pinning factor (S) was plotted as a function of the 2D semiconductor's band gap (**Figure 11**). With the band gap decreasing, the S value generally becomes smaller. The linear relationship between the pinning factor and the band gap is obvious ($R^2 = 0.96$, where R is the linear correlation coefficient) when ML MoS_2 and black phosphorene are not taken into account. The phenomenon is attributed to the more concentrated distribution of the MIGS with the band gap shrinking. A more concentrated distribution of the MIGS leads to a more concentrated distribution of the Fermi levels and thus a more concentrated SBH. As a result, a smaller S is obtained from the definition of pinning factor ($S = d\Phi_{SB}/dW_M$). An uncommonly strong FLP is found at the lateral interface of ML MoS_2 SBFET by the experiment,[52] contrary to the uncommonly weak FLP effect in black phosphorene SBFET by the theoretical calculation.[29] When taking ML MoS_2 and black phosphorene into consideration, the linear coefficient R^2 becomes 0.69.

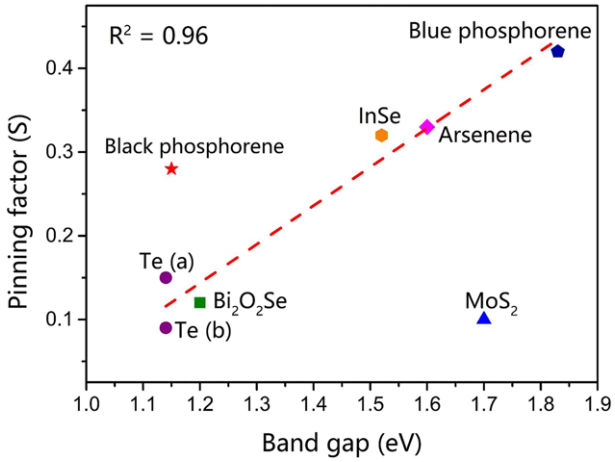

Figure 11. Pinning factor (S) as a function of ML 2D semiconductor's band gap by theoretical work.[48–52] a) Te and b) Te represent the pinning factor at different directions. The red line is the fitting line, and R is the linear correlation coefficient without the inclusion of ML MoS_2 and black phosphorene.

5. Conclusion

In conclusion, the interfacial properties of the sub-5 nm ML Bi_2O_2Se Schottky-barrier FETs with a sequence of common metal electrodes (Au, Pd, Pt, Ag, Sc, and Ti) are systematically studied by using ab initio quantum transport simulations. There is no vertical SBH because of the metallization of ML Bi_2O_2Se under the contact metal. On account of a usually strong within-gap FLP due to the MIGS or the electrode's Fermi-level modification at the interface, a lateral n-type Schottky contact is formed with Au, Pd, and Ag electrodes, featured by an S_1 of −0.07. Fortunately, with the unusual beyond-gap FLP mainly owing to the electrode's Fermi-level modification at the interface, a desirable lateral n-type ohmic contact is obtained with Pt, Sc, and Ti electrodes, featuring an $S_2 = 0.05$, making up for the lack of ohmic contact in the

experiment. In addition to figuring out the interfacial properties of the ML Bi_2O_2Se device, the research is instructive for further experiments.

Supporting Information

Supporting Information is available from the Wiley Online Library or from the author.

Acknowledgements

S.L. and L.X. contributed equally to this work. This work was supported by the National Natural Science Foundation of China (No. 11674005/11664026/11804140) and the Ministry of Science and Technology (Nos. 2016YFB0700600 [National Materials Genome Project] and 2016YFA0301300) of China. L.X. was also funded by the Key Research and Development Program of Ningxia (No. 2018BEE03023), the Natural Science Foundation of Ningxia (No. 2018AAC03236), the Higher School Scientific Research Project of Ningxia Department of Education (No. NGY2018-130), the Key Scientific Research Project of Ningxia Normal University (No. NXSFZDA1807), and the Youth Talent Support Program of Ningxia, China (2016). The authors thank Dr. Jinxiong Wu (Hailin Peng's group) for his professional and patient explanations on the experimental Bi_2O_2Se transistor.

Conflict of Interest

The authors declare no conflict of interest.

Keywords

density functional theory, field-effect transistor, interfacial property, monolayer Bi_2O_2Se, quantum transport simulations

Received: November 12, 2018
Revised: February 4, 2019
Published online: February 26, 2019

[1] R. F. Service, *Science* **2009**, *323*, 1000.
[2] D. Xiang, X. L. Wang, C. C. Jia, T. Lee, X. F. Guo, *Chem. Rev.* **2016**, *116*, 4318.
[3] H. Jeong, D. Kim, G. Wang, S. Park, H. Lee, K. Cho, W. T. Hwang, M. H. Yoon, Y. H. Jang, H. Song, D. Xiang, T. Lee, *Adv. Funct. Mater.* **2014**, *24*, 2472.
[4] G. Fiori, F. Bonaccorso, G. Iannaccone, T. Palacios, D. Neumaier, A. Seabaugh, S. K. Banerjee, L. Colombo, *Nat. Nanotechnol.* **2014**, *9*, 768.
[5] J. Kang, W. Liu, D. Sarkar, D. Jena, K. Banerjee, *Phys. Rev. X* **2014**, *4*, 031005.
[6] F. Schwierz, J. Pezoldt, R. Granzner, *Nanoscale* **2015**, *7*, 8261.
[7] Z. Y. Ni, M. Ye, J. H. Ma, Y. Y. Wang, R. G. Quhe, J. X. Zheng, L. Dai, D. P. Yu, J. J. Shi, J. B. Yang, S. Watanabe, J. Lu, *Adv. Electron. Mater.* **2016**, *2*, 1600191.
[8] M. Z. Rahman, C. W. Kwong, K. Davey, S. Z. Qiao, *Energy Environ. Sci.* **2016**, *9*, 709.
[9] J. Wu, H. Yuan, M. Meng, C. Chen, Y. Sun, Z. Chen, W. Dang, C. Tan, Y. Liu, J. Yin, Y. Zhou, S. Huang, H. Q. Xu, Y. Cui, H. Y. Hwang, Z. Liu, Y. Chen, B. Yan, H. Peng, *Nat. Nanotechnol.* **2017**, *12*, 530.
[10] C. Chen, M. Wang, J. Wu, H. Fu, H. Yang, Z. Tian, T. Tu, H. Peng, Y. Sun, X. Xu, J. Jiang, N. B. M. Schroter, Y. Li, D. Pei, S. Liu, S. A. Ekahana, H. Yuan, J. Xue, G. Li, J. Jia, Z. Liu, B. Yan, H. Peng, Y. Chen, *Sci. Adv.* **2018**, *4*, eaat8355.
[11] J. Yu, Q. Sun, *Appl. Phys. Lett.* **2018**, *112*, 053901.
[12] J. Wu, Y. Liu, Z. Tan, C. Tan, J. Yin, T. Li, T. Tu, H. Peng, *Adv. Mater.* **2017**, *29*, 1704060.
[13] A. Allain, J. H. Kang, K. Banerjee, A. Kis, *Nat. Mater.* **2015**, *14*, 1195.
[14] H. Liu, Y. C. Du, Y. X. Deng, P. D. Ye, *Chem. Soc. Rev.* **2015**, *44*, 2732.
[15] S. Banerjee, J. Rowland, O. Erten, M. Randeria, *Phys. Rev. X* **2014**, *4*, 031045.
[16] C. Gong, L. Colombo, R. M. Wallace, K. Cho, *Nano Lett.* **2014**, *14*, 1714.
[17] Y. Z. Guo, D. M. Liu, J. Robertson, *ACS Appl. Mater. Interfaces* **2015**, *7*, 25709.
[18] I. Popov, G. Seifert, D. Tomanek, *Phys. Rev. Lett.* **2012**, *108*, 156802.
[19] H. Zhong, R. Quhe, Y. Wang, Z. Ni, M. Ye, Z. Song, Y. Pan, J. Yang, L. Yang, M. Lei, J. Shi, J. Lu, *Sci. Rep.* **2016**, *6*, 21786.
[20] X. Y. Zhang, Y. Y. Pan, M. Ye, R. Quhe, Y. Y. Wang, Y. Guo, H. Zhang, Y. Dan, Z. G. Song, J. Z. Li, J. B. Yang, W. L. Guo, J. Lu, *Nano Res.* **2018**, *11*, 707.
[21] R. Quhe, J. Liu, J. Wu, J. Yang, Y. Wang, Q. Li, T. Li, Y. Guo, J. Yang, H. Peng, M. Lei, J. Lu, *Nanoscale* **2019**, *11*, 532.
[22] J. Yang, R. Quhe, Q. Li, S. Liu, Y. Pan, X. Zhang, J. Li, J. Yan, B. Shi, H. Pang, L. Xu, Z. Zhang, F. Pan, J. Lu, J. Yang, *Adv. Electron. Mater.* **2019**, 1800720.
[23] D. J.Cheng, G. Barcaro, J. C. Charlier, M. Hou, A. Fortunelli, *J. Phys. Chem. C* **2011**, *115*, 10537.
[24] C. So, H. Zhang, Y. Y. Wang, M. Ye, Y. Y. Pan, R. G. Quhe, J. Z. Li, X. Y. Zhang, Y. S. Zhou, J. Lu, *Phys. Status Solidi B* **2017**, *254*, 1600837.
[25] Y. K. Yuan, R. G. Quhe, J. X. Zheng, Y. Y. Wang, Z. Y. Ni, J. J. Shi, J. Lu, *Physica E* **2014**, *58*, 38.
[26] Y. Y. Wang, J. Z. Li, J. H. Xiong, Y. Y. Pan, M. Ye, Y. Guo, H. Zhang, R. Quhe, J. Lu, *Phys. Chem. Chem. Phys.* **2016**, *18*, 19451.
[27] Y. Pan, Y. Dan, Y. Wang, M. Ye, H. Zhang, R. Quhe, X. Zhang, J. Li, W. Guo, L. Yang, J. Lu, *ACS Appl. Mater. Interfaces* **2017**, *9*, 12694.
[28] Y. Y. Pan, S. B. Li, M. Ye, R. G. Quhe, Z. G. Song, Y. Y. Wang, J. X. Zheng, F. Pan, W. L. Guo, J. B. Yang, J. Lu, *J. Phys. Chem. C* **2016**, *120*, 13063.
[29] Y. Y. Pan, Y. Y. Wang, M. Ye, R. G. Quhe, H. X. Zhong, Z. G. Song, X. Y. Peng, D. P. Yu, J. B. Yang, J. J. Shi, J. Lu, *Chem. Mater.* **2016**, *28*, 2100.
[30] Y. Y. Wang, R. X. Yang, R. Quhe, H. X. Zhong, L. X. Cong, M. Ye, Z. Y. Ni, Z. G. Song, J. B. Yang, J. J. Shi, J. Li, J. Lu, *Nanoscale* **2016**, *8*, 1179.
[31] P. E. Blochl, *Phys. Rev. B* **1994**, *50*, 17953.
[32] G. Kresse, D. Joubert, *Phys. Rev. B* **1999**, *59*, 1758.
[33] G. Kresse, J. Hafner, *Phys. Rev. B* **1993**, *47*, 558.
[34] G. Kresse, J. Furthmuller, *Phys. Rev. B* **1996**, *54*, 11169.
[35] G. Kresse, J. Hafner, *Phys. Rev. B* **1994**, *49*, 14251.
[36] H. J. Monkhorst, J. D. Pack, *Phys. Rev. B* **1976**, *13*, 5188.
[37] M. Brandbyge, J. L. Mozos, P. Ordejon, J. Taylor, K. Stokbro, *Phys. Rev. B* **2002**, *65*, 165401.
[38] D. R. Smith, S. Schultz, P. Markos, C. M. Soukoulis, *Phys. Rev. B* **2002**, *65*, 195104.
[39] J. M. Soler, E. Artacho, J. D. Gale, A. Garcia, J. Junquera, P. Ordejon, D. Sanchez-Portal, *J. Phys. Condens. Matter* **2002**, *14*, 2745.
[40] J. P. Perdew, K. Burke, M. Ernzerhof, *Phys. Rev. Lett.* **1997**, *78*, 1396.
[41] R. Quhe, R. Fei, Q. Liu, J. Zheng, H. Li, C. Xu, Z. Ni, Y. Wang, D. Yu, Z. Gao, J. Lu, *Sci. Rep.* **2012**, *2*, 853.
[42] Y. Liang, L. Yang, *Phys. Rev. Lett.* **2015**, *114*, 063001.
[43] Y. Zhang, T. R. Chang, B. Zhou, Y. T. Cui, H. Yan, Z. Liu, F. Schmitt, J. Lee, R. Moore, Y. Chen, H. Lin, H. T. Jeng, S. K. Mo, Z. Hussain, A. Bansil, Z. X. Shen, *Nat. Nanotechnol.* **2014**, *9*, 111.

[44] S. Liu, J. Li, B. Shi, X. Zhang, Y. Pan, M. Ye, R. Quhe, Y. Wang, H. Zhang, J. Yan, L. Xu, Y. Guo, F. Pan, J. Lu, *J. Mater. Chem. C* **2018**, *6*, 5651.
[45] J. Zheng, Y. Wang, L. Wang, R. Quhe, Z. Ni, W. N. Mei, Z. Gao, D. Yu, J. Shi, J. Lu, *Sci. Rep.* **2013**, *3*, 2081.
[46] Y. Liu, J. Guo, E. Zhu, L. Liao, S. J. Lee, M. Ding, I. Shakir, V. Gambin, Y. Huang, X. Duan, *Nature* **2018**, *557*, 696.
[47] L. Xu, S. Liu, J. Yang, B. Shi, Y. Pan, X. Zhang, H. Li, J. Yan, J. Li, L. Xu, J. Yang, J. Lu, unpublished.
[48] J. Yan, X. Zhang, Y. Pan, J. Li, B. Shi, S. Liu, J. Yang, Z. Song, H. Zhang, M. Ye, R. Quhe, Y. Wang, J. Yang, F. Pan, J. Lu, *J. Mater. Chem. C* **2018**, *6*, 6153.
[49] B. Shi, Y. Wang, J. Li, X. Zhang, J. Yan, S. Liu, J. Yang, Y. Pan, H. Zhang, J.-B. Yang, F. Pan, J. Lu, *Phys. Chem. Chem. Phys.* **2018**, *20*, 24641.
[50] Y. Wang, M. Ye, M. Weng, J. Li, X. Zhang, H. Zhang, Y. Guo, Y. Pan, L. Xiao, J. Liu, F. Pan, J. Lu, *ACS Appl. Mater. Interfaces* **2017**, *9*, 29273.
[51] J. Li, X. Sun, C. Xu, X. Zhang, Y. Pan, M. Ye, Z. Song, R. Quhe, Y. Wang, H. Zhang, Y. Guo, J. Yang, F. Pan, J. Lu, *Nano Res.* **2018**, *11*, 1834.
[52] C. Kim, I. Moon, D. Lee, M. S. Choi, F. Ahmed, S. Nam, Y. Cho, H. J. Shin, S. Park, W. J. Yoo, *ACS Nano* **2017**, *11*, 1588.